

Dual-band combined-aperture variable inclination continuous transverse stub antenna with consistent beam direction

Lu, Yunlong; You, Yang; Wang, Yi; Zheng, Zi Wei; Huang, Jifu

DOI:

[10.1109/TAP.2022.3177502](https://doi.org/10.1109/TAP.2022.3177502)

License:

Other (please specify with Rights Statement)

Document Version

Peer reviewed version

Citation for published version (Harvard):

Lu, Y, You, Y, Wang, Y, Zheng, ZW & Huang, J 2022, 'Dual-band combined-aperture variable inclination continuous transverse stub antenna with consistent beam direction', *IEEE Transactions on Antennas and Propagation*. <https://doi.org/10.1109/TAP.2022.3177502>

[Link to publication on Research at Birmingham portal](#)

Publisher Rights Statement:

Y. Lu, Y. You, Y. Wang, Z. -W. Zheng and J. Huang, "Dual-Band Combined-Aperture Variable Inclination Continuous Transverse Stub Antenna with Consistent Beam Direction," in *IEEE Transactions on Antennas and Propagation*, doi: 10.1109/TAP.2022.3177502.

© 2021 IEEE. Personal use of this material is permitted. Permission from IEEE must be obtained for all other uses, in any current or future media, including reprinting/republishing this material for advertising or promotional purposes, creating new collective works, for resale or redistribution to servers or lists, or reuse of any copyrighted component of this work in other works.

General rights

Unless a licence is specified above, all rights (including copyright and moral rights) in this document are retained by the authors and/or the copyright holders. The express permission of the copyright holder must be obtained for any use of this material other than for purposes permitted by law.

- Users may freely distribute the URL that is used to identify this publication.
- Users may download and/or print one copy of the publication from the University of Birmingham research portal for the purpose of private study or non-commercial research.
- User may use extracts from the document in line with the concept of 'fair dealing' under the Copyright, Designs and Patents Act 1988 (?)
- Users may not further distribute the material nor use it for the purposes of commercial gain.

Where a licence is displayed above, please note the terms and conditions of the licence govern your use of this document.

When citing, please reference the published version.

Take down policy

While the University of Birmingham exercises care and attention in making items available there are rare occasions when an item has been uploaded in error or has been deemed to be commercially or otherwise sensitive.

If you believe that this is the case for this document, please contact UBIRA@lists.bham.ac.uk providing details and we will remove access to the work immediately and investigate.

Dual-Band Combined-Aperture Variable Inclination Continuous Transverse Stub Antenna with Consistent Beam Direction

Yunlong Lu, *Member, IEEE*, Yang You, Yi Wang, *Senior Member, IEEE*, Zi-Wei Zheng, and Jifu Huang

Abstract— This paper presents a Tx/Rx dual-band combined-aperture variable inclination continuous transverse stub (VICTS) antenna for low-earth-orbit Satellite-on-the-Move (SOTM) applications. The beam directions for the Tx and Rx bands are kept consistent during beam scanning, so that the antenna allows a duplex link. The topology of the combined-aperture VICTS antenna is derived from the requirement for consistent beam directions. Non-uniform slow-wave structures are used to achieve the required phase difference and phase-changing rate between the radiation slots in the two bands, while maximizing the antenna efficiency. Pre-deflection technique is applied to the radiation slots to reduce the gain drop at a wide beam scanning angle. A prototype operating at K- and Ka-bands is designed, fabricated and measured. Experimental results show that the antenna has a consistent beam direction during scanning in the frequency ranges of 19-21 GHz (Rx band) and 29-31 GHz (Tx band). The maximum beam directions in Tx and Rx bands exceeds $\pm 47^\circ$ at a relative rotation angle of 40° , and the gain drop during the beam scanning is reduced within 2.3 dB and 3.5 dB.

Keywords—Variable inclination continuous transverse stub antenna, beam scanning, millimeter wave antennas, Satellite-on-the-move (SOTM), dual-band antennas.

I. INTRODUCTION

Recently, vehicle-to-everything (V2X) communication has attracted much attention [1]. Satellite-on-the-move (SOTM) is one key enabling technology, especially in areas that are not well covered by cellular networks [2]. With the rapid deployment of low-earth-orbit (LEO) satellite communication programs, the demand for LEO SOTM applications has increased rapidly [3], [4]. Compared with the lower frequency bands of C- and Ku-bands [5], [6], the use of higher frequency bands in LEO satellite communications has the advantages of

This work was supported partly National Natural Science Foundation of China under Projects 62171242, U1809203, 61801252, and 61631012, in part by Zhejiang Provincial Natural Science Foundation of China under Project LY21F010002 and Natural Science Foundation of Ningbo under Project 202003N4108. (*Corresponding author: Yunlong Lu.*)

Y. Lu, Y. You, and J. Huang are with the Faculty of Electrical Engineering and Computer Science, Ningbo University, Ningbo, Zhejiang, 315211, China (e-mail: luyunlong@nbu.edu.cn).

Y. Wang is with School of Engineering, University of Birmingham, B15 2TT, United Kingdom (e-mail: y.wang.1@bham.ac.uk).

Z.-W. Zheng is with Digital Industry Research Institute, Zhejiang Wanli University, Ningbo, Zhejiang, 315100, P. R. China.

system throughput, terminal size and mobility [7], [8]. For example, K- and Ka-bands (17.7-21.2 GHz and 27.5-31 GHz) have been adopted in LEO satellite communications to establish down- and up-links [9]-[12]. The antenna mounted on the mobile vehicular platform should have low-profile, low-cost and capability of beam-scanning [13]-[20].

Phased-array antenna is considered to be one of the most promising radio architectures with a low profile and flexible beam-scanning configuration capability [19], [22]. But it suffers from prohibitively high cost and relative high loss in K- and Ka-bands. Mechanical beam scanning solution is attractive for ground mobile platform (including airplanes) antenna system for SOTM applications, due to its lower cost and mechanical robustness [14], [21]. Conventional parabolic antenna is commonly used in satellite communications, but it is limited by its bulky structure [22], [23].

Continuous transverse stub (CTS) antenna, as a good candidate for high-performance antenna systems, has been increasingly widely used in many applications [24]-[30]. The variable inclination CTS (VICTS) antenna that provided 2-D beam-scanning with a low profile and high efficiency has been furtherly concerned by both the academia and industry for SOTM systems [31]-[35]. The VICTS antenna is a series-fed CTS antenna, which consists of an upper radiation CTS plate and a lower feed network plate [32]-[34]. Its 2-D beam scanning is achieved by mechanical rotating these two plates both in horizontal plane with unequal speed. Conventionally, one VICTS antenna only operates at a single band and requires a group of servos to control the beam scanning. Limited by the operating bandwidth of series-fed CTS antenna structure [35], it has been difficult to employ single VICTS antenna to cover both K- and Ka-bands. Therefore, to realize a duplex communication, two separated VICTS antennas are often used for down- and up-links, respectively. This configuration doubles the required servo systems, thereby increasing the cost and power consumption. To overcome this disadvantage, a shared-aperture VICTS antenna supporting dual-band operating is the way to go but remains a design challenge. In [36], a dual-band shared-aperture VICTS antenna is reported. With two independent feed networks at K- and Ka-bands to excite shared CTS radiation slots, the VICTS antenna operates at 19.5-20.1 GHz and 28.8-29.6 GHz with a peak gain over 22 dBi. However, the beam directions in the two frequency bands

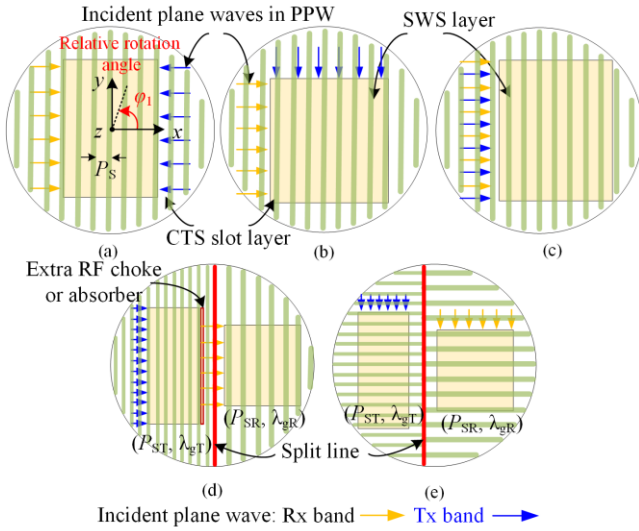


Fig. 1. Topologies of dual-band VICTS shared-aperture with (a) face-to-face excitation, (b) orthogonal excitation and (c) one-side excitation; Combined-aperture with one-side excitation (d) perpendicular to the split line and (e) along the split line.

deviate greatly during the beam scanning. This makes the design unsuitable for tracking and establishing a duplex link with a single satellite. For LEO SOTM applications, the antenna peak gain should be commonly maintained over 20 dBi during the beam scanning and the beam direction deviation between the Tx and Rx bands should be as small as possible. For example, no more than the minimum 1-dB beam-width, so that the cross-level of the radiation patterns between the Tx and Rx beams will be within the 1-dB gain reduction. This will allow a stable duplex link.

This paper aims to tackle this challenge and presents a new Tx/Rx dual-band combined-aperture VICTS antenna. The radiating parts in Tx and Rx bands are loaded with non-uniform slow-wave structure (SWS) to adjusting the phase difference and phase-changing rate (PCR) between the adjacent radiation slots in a wideband. The PCR is defined as the ratio of phase difference to the frequency difference. This is the feature that ensures the phase relation for consistent beam direction between the Tx and Rx bands during beam scanning can be satisfied. Combined with the arrangement of pre-deflection radiation slots, the gain variation during beam scanning has been reduced. Two novel 1-to-3 E-planar power dividers with equal-amplitude and in-phase response are adopted in the Tx and Rx feeding circuits to realize compact and high-performance plane-wave generators (PWGs). With these unique features, this design could find great potentials for LEO SOTM applications. The paper is organized as follows: Section II describes the operating principle, and the detailed analysis and design are discussed in Section III. Section IV gives the experimental validation, followed by conclusions in Section V.

II. OPERATION PRINCIPLE

Since the CTS radiating structure supports a wide frequency band, the challenge of the dual-band shared-aperture VICTS lies in the dual-band feed network. According to the operating principle of the VICTS antenna [32]-[36], there are three

potential excitation ways to achieve the dual-band operation: face-to-face, orthogonal and one-side excitations, as shown in Fig. 1(a), (b) and (c). It should be noted that only the simplified topology is presented. In order to avoid the grating lobes, the period (P_s) of the CTS radiation slots is less than one free-space wavelength corresponding to the highest operating frequency. The SWS is usually loaded underneath the radiation slots to shorten the effective guided wavelength in the parallel-plate waveguide (PPW) [35], so that the initial beam can be controlled near $\theta=0^\circ$ (improving the beam scanning range). The face-to-face and orthogonal excitations were discussed in [36]. When the CTS slot layer and the SWS layer rotate relative to each other, it is difficult to keep the same phase gradient in the two frequency bands. This leads to inconsistent beam directions during the beam scanning between the two frequency bands. For this reason, these two topologies are not suitable for Tx/Rx shared-aperture applications, where the beam is required to point to the same object.

To overcome this drawback, the incident waves at the two frequencies (f_R and f_T for Rx and Tx) can be arranged on the same side. Assume the entire radiation aperture is excited for both bands, as shown in Fig. 1(c). When the relative rotation angle is φ_1 , the beam direction (θ, φ) can be determined by the following equation [35], [37].

$$\left(\frac{\lambda_g}{\lambda_0}\right)^2 \sin^2(\theta) = \left[\cos(\varphi_1) - \frac{\lambda_g}{P_s}\right]^2 + \sin^2(\varphi_1) \quad (1-1)$$

$$\tan(\varphi) = \frac{\sin(\varphi_1)}{\cos(\varphi_1) - \frac{\lambda_g}{P_s}} \quad (1-2)$$

where λ_g, λ_0 are the effective guided wavelength (in the PPW) and free-space wavelength, respectively. For a fixed relative rotation angle (φ_1) and radiation slot period (P_s), the beam direction in azimuth plane is only related with λ_g , while the beam direction in the elevation plane is determined by both λ_g and λ_0 . To achieve the same beam directions at f_R and f_T in the azimuth plane, from equation (1-2), it is required that $\lambda_{gT} = \lambda_{gR}$. The relation $\lambda_{gT}/\lambda_{0T} = \lambda_{gR}/\lambda_{0R}$ should be further guaranteed to achieve the same beam directions in elevation plane, according to the equation (1-1). $\lambda_{g(T/R)}$ and $\lambda_{0(T/R)}$ are the effective guided wavelength and free-space wavelength at $f_{(T/R)}$. In addition, considering the initial beam direction needs to be around $\theta=0^\circ$, λ_g should be as close to the period (P_s) as possible. Therefore, it is difficult to design a SWS to meet these requirements.

One solution to achieve consistent beam directions for the dual-band operation is to excite a combined-aperture (as opposed to a shared aperture) with the two incident plane waves from one-side. Two such topologies with different excitation structures are shown in Fig. 1(d) and (e). The split line divides the radiation slots and SWS into two parts. Each part operates at a different frequency. P_{ST} and P_{SR} represents the periods of the radiation slots in the Tx and Rx parts. The two parts are independently excited. The separated SWSs can obtain the desired guided wavelengths in different frequency bands. Combined with the unequal radiation slot periods, the

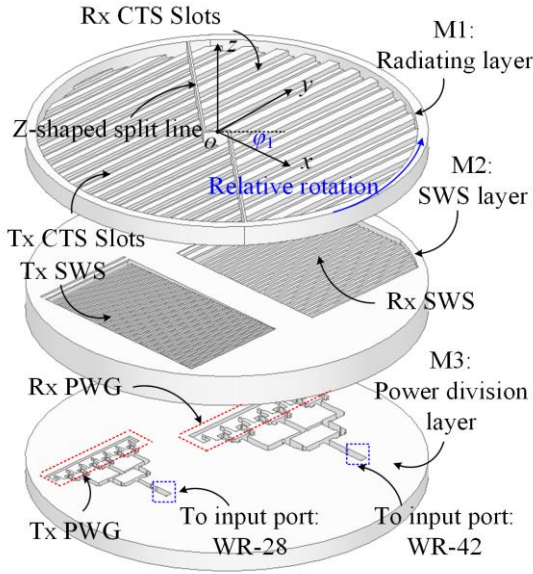


Fig. 2. Antenna configuration.

consistent beam direction during scanning can be achieved in a wide Tx and Rx bands.

Although both topologies (Fig. 1(d) and (e)) are usable, there is one shortcoming in the structure shown in Fig. 1(d). Since the two sets of incident plane waves are arranged front and back along the propagation direction of the electromagnetic (EM) waves, it requires an extra RF choke or absorbing material to be loaded at one of the radiating parts to prevent mutual interference between the incident plane waves at different frequencies. The topology in Fig. 1(e) avoids this problem. Since the two incident plane waves are arranged side by side, there is no overlapped region where the generated EM waves propagate. This topology is utilized in this work.

III. ANALYSIS AND DESIGN

A. Configuration

The configuration of the dual-band combined-aperture VICTS is shown in Fig. 2. The diameter of the whole antenna is 180 mm. It consists of two parts: the radiating part in layer M1 and the feeding part in M2 and M3. The Z-shaped splitting line divides the radiating part into two areas: one for the Tx band and the other for the Rx band. Two groups of multiple CTS radiation slots are used for each band. The CTS radiation slots are deflected at a certain angle to reduce the gain variation during beam scanning (to be discussed in Section III-B). For each band, the feeding part contains non-uniform SWSs and PWGs, which excite the radiation slots in series. Two standard waveguide input ports, i.e., WR-28 and WR-42, are located at the back-side of the power division layer. To establish a stable duplex LEO SOTM link, it is necessary to have a wide beam scanning range with consistent beam direction in both bands. The specifications of the proposed VICTS antenna are tabulated in Table I. Due to the beam squint caused by the frequency shift in the VICTS antenna, a frequency correspondence between the Tx and Rx bands, commonly used in high-throughput satellite communications [38], is employed

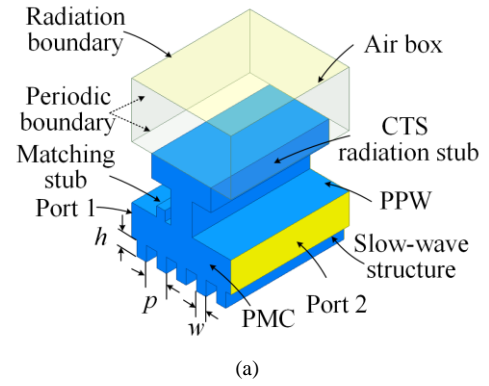


Fig. 3. Air models of SWS loaded CTS units. (a) 3-D view of common structure; (b) side-view of the unit in Tx band; (c) side-view of the unit in Rx band. All dimensions are given in millimeters.

TABLE I
SPECIFICATION OF THE COMBINED-APERTURE VICTS ANTENNA

Frequency band	Tx band (up-link)	29-31 GHz
	Rx band (down-link)	19-21 GHz
Beam scanning range in elevation plane	>45°	
Peak gain	Tx band (up-link)	>24 dBi
	Rx band (down-link)	>20 dBi
Reflection coefficient	<-10 dB	
Initial beam direction	<10° (or -10°)	
Consistent beam directions between the Tx and Rx bands	$\theta(19 \text{ GHz}) = \theta(29 \text{ GHz})$	
	$\theta(20 \text{ GHz}) = \theta(30 \text{ GHz})$	
	$\theta(21 \text{ GHz}) = \theta(31 \text{ GHz})$	
Dimensions	Diameter \leq 180 mm	

here to obtain the consistent beam direction. In addition, the equal and large bandwidth (2 GHz) in Tx and Rx bands is only considered here to validate the design methodology. It may not be the same in different practical application scenarios. However, a consistent beam direction within certain tolerance can still be obtained using the design method described in the following sections. For example, even when the bandwidth is small (less than 500 MHz), it is sufficient to consider the consistent beam direction between the center frequencies of the Tx and Rx bands, since the beam direction deviation does not normally exceed 1-dB beam-width [37].

B. Radiating Part with SWS Loaded

As the relative rotation angle is the same for both apertures, once (1) is satisfied at one specific rotation angle, consistent beam direction can be guaranteed during beam scanning. The initial beams in the Tx and Rx bands are firstly analyzed.

1) Initial beams

The initial beam is when the CTS slot is perpendicular to the

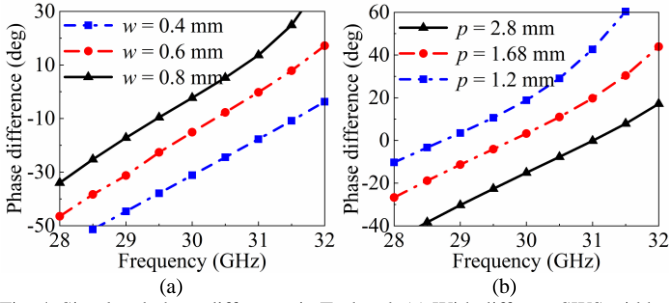


Fig. 4. Simulated phase difference in Tx-band. (a) With different SWS widths; (b) with different SWS periods.

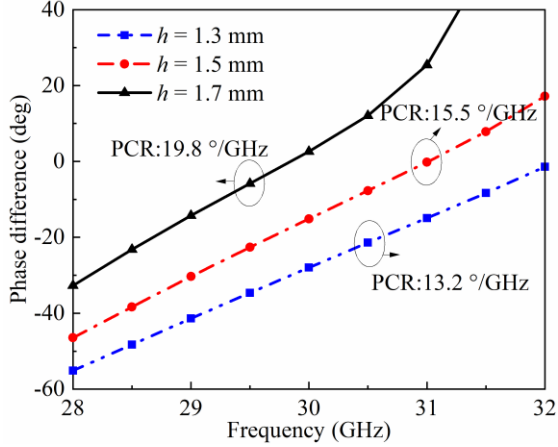


Fig. 5. PCRs with different SWS depths in Tx-band.

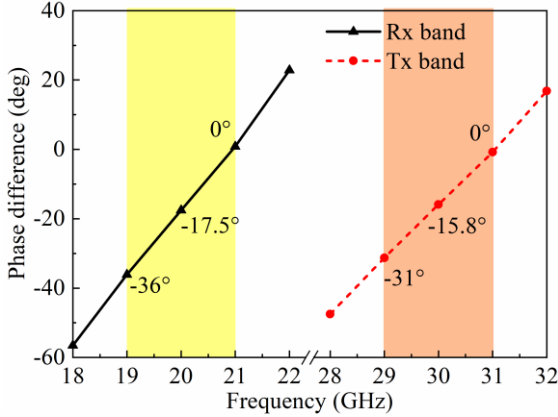


Fig. 6. Optimized phase difference in Tx and Rx bands.

propagation direction of the excitation. Fig. 3(a) shows the 3-D view of the SWS loaded CTS unit at $\phi_1=0^\circ$. The match stub is used to improve the impedance matching between the PPW and the CTS slot. The period is chosen to avoid the grating lobe during beam scanning in the Tx/Rx band. $P_{ST}=8.4$ mm and $P_{SR}=12.6$ mm are used. The two separate SWSs underneath the Tx and Rx CTS slots are used to control the initial beam direction, as shown in Fig. 3(b) and (c).

Because the operating principles of the two SWSs are the same, only the Tx band SWS is analyzed here. The effective guided wavelength depends on the SWS depth (h), width (w) and period (p) [35], as shown in Fig. 3(a). So does the phase difference between the adjacent CTS slots. Fig. 4 plots the simulated phase difference versus different values of w and p . It can be seen that the phase difference in the Tx band can be

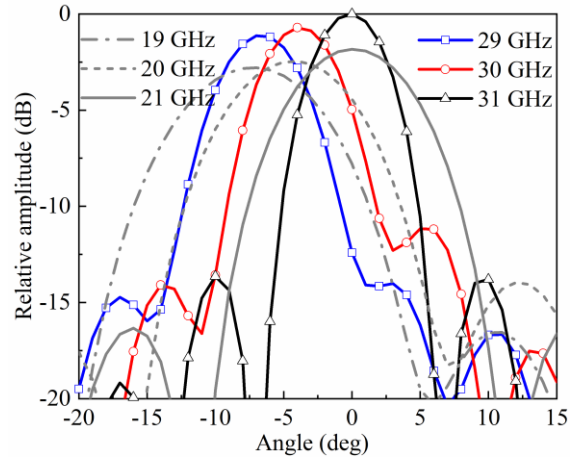


Fig. 7. Simulated normalized radiation patterns of the initial beams in Tx and Rx bands.

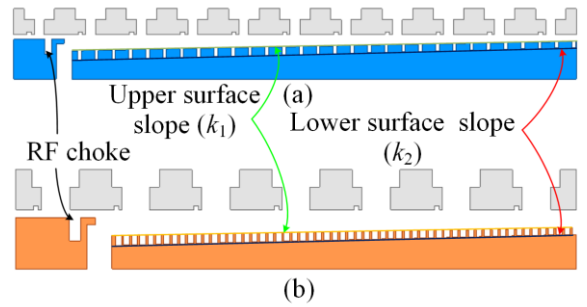


Fig. 8. Structure of non-uniform SWS. (a) Tx band; (b) Rx band.

adjusted by changing the width and period of the SWS.

However, the PCRs are slightly different. The requirement for consistent initial beam direction dictates that adjustment has to be made within a certain range. This can be done by changing the depth of SWS. Fig. 5 illustrates that when the depth (h) changes from 1.3 mm to 1.7 mm, the PCR of 13.2 - 19.8 °/GHz can be obtained. This shows that with the SWS period, width and depth, the phase difference and the PCR between the adjacent CTS slots can be flexibly controlled.

According to the specifications in Table I, the optimized dimensions of the SWS in Tx and Rx bands are shown in Fig. 3(b) and (c), respectively. Fig. 6 plots the extracted phase difference in Tx and Rx bands. Although the PCRs are not perfectly matched, the maximum phase difference is less than 5° (occurring between 19 GHz and 29 GHz). Fig. 7 shows the normalized radiation patterns of the initial beams at the Tx and Rx bands. The beam directions of the initial beams are all restricted within $\theta=10^\circ$. The deviation of the initial beam direction between the Tx and Rx bands does not exceed 1° , which is less than the 1-dB beam-width. The beams are considered to be consistent.

2) Beam Scanning

To maximize the antenna efficiency, an equal amplitude excitation among the radiation slots is required. This is achieved by adjusting the slopes (k_1 and k_2) of the non-uniform SWS, as shown in Fig. 8. An RF choke is placed near one end of the SWS to prevent the plane wave from propagating in the opposite direction. The detailed design of the non-uniform

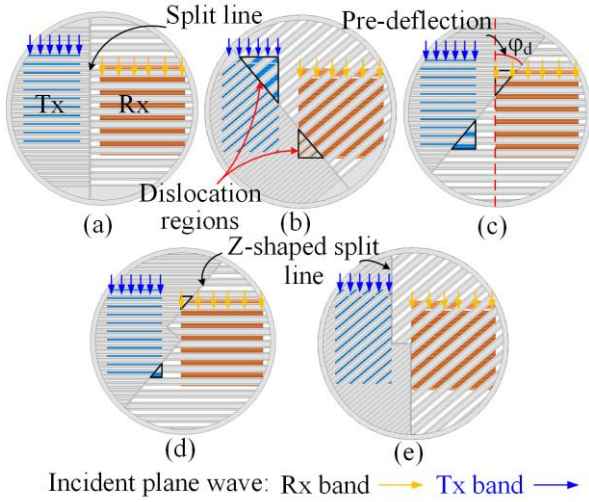


Fig. 9. Different method of combination. (a) Conventional combination without relative rotation; (b) conventional combination with relative rotation; (c) combination with pre-deflection radiation slots; (d) combination with Z-shaped split line at $\phi_1=0^\circ$; (e) combination with Z-shaped split line at $\phi_1=40^\circ$.

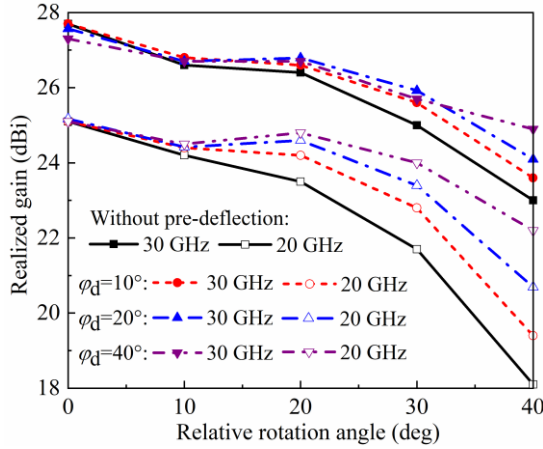


Fig. 10. Gain comparison with and without pre-deflection at 20 GHz and 30 GHz.

SWS can be found in [26]. In this work, the slope k_1/k_2 is optimized to achieve equal amplitude distribution at the center frequencies of the Tx and Rx bands. They are 0.018/0.025 and 0.017/0.024 for the Tx and Rx, respectively.

The optimized CTS slots and non-uniform SWS are combined to implement the combined-aperture VICTS. The conventional combination is shown in Fig. 9(a). This offers the highest peak gain in the initial beam. However, this structure will produce dislocation regions when the relative rotation angle (ϕ_1) increases, as shown in Fig. 9(b). Unwanted signals generated by adjacent PWG can enter from this dislocation region, causing interference. This region becomes larger with increasing ϕ_1 and therefore the effective apertures in the Tx and Rx bands are reduced. This will aggravate the gain drop at a wide beam angle.

To solve this problem, a pre-deflection technology is introduced to the CTS radiation slots, as shown in Fig. 9(c). Note that the CTS slot is still perpendicular to the plane wave propagation at $\phi_1=0^\circ$ but dislocation region is deliberately inserted. It gradually decreases with increasing ϕ_1 . To further

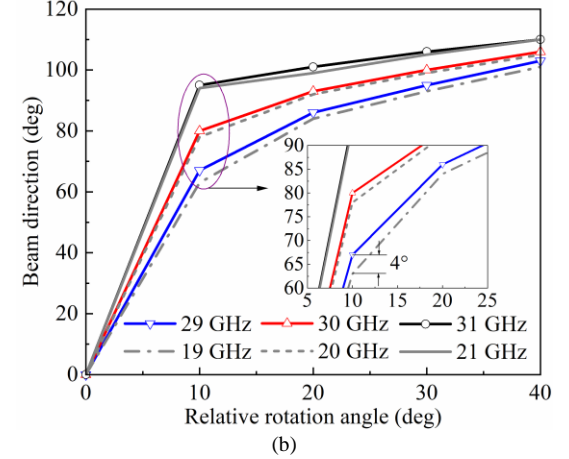
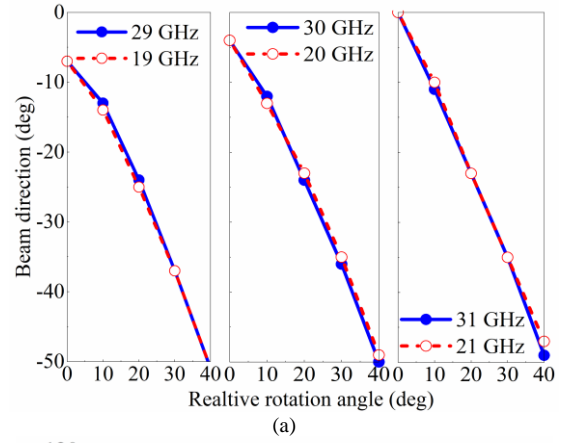


Fig. 11. Simulated beam directions with different relative rotation angles. (a) Elevation plane; (b) azimuth plane.

minimize the influence of the dislocation region on the initial beam, the split line is bent into a Z-shape to compress the overlapped area, as shown in Fig. 9(d). Compared with Fig. 9(a), the effective aperture in Fig. 9(d) for the initial beams in the Tx band is slightly smaller, while it has almost no effect on the Rx band. With increasing ϕ_1 , the effective aperture in Tx band becomes larger, while the effective aperture in Rx band remains stable. This effectively reduces the gain drop and potentially improves the signal-to-noise ratio of the communication link at a wide beam scanning angle. Fig. 10 compares the peak gain with and without pre-deflection at the center frequencies of Tx and Rx bands. As the pre-deflection angle (ϕ_d) increases, the peak gain of the initial beam in Tx band is slightly sacrificed, while this does not affect the Rx band. This is consistent with the previous analysis. The peak gains in both the Tx and Rx bands gradually rise at $\phi_1=40^\circ$, reducing the gain difference between $\phi_1=0^\circ$ and 40° . When $\phi_d=40^\circ$, the minimum gain differences are 2.3 dB and 2.9 dB in Tx and Rx bands. Since the beam direction in elevation plane, when $\phi_1=40^\circ$, reaches more than -45° (see Fig. 11), this work adopts the CTS radiation slots with pre-deflection angle of $\phi_d=40^\circ$ to realize the minimum gain variation during beam scanning. This also means that there is no dislocation region in this case when ϕ_1 is 40° , as shown in Fig. 9(e).

Fig. 11 shows the simulated beam directions in the Tx and Rx bands. When $\phi_1=40^\circ$, the beam direction in elevation plane

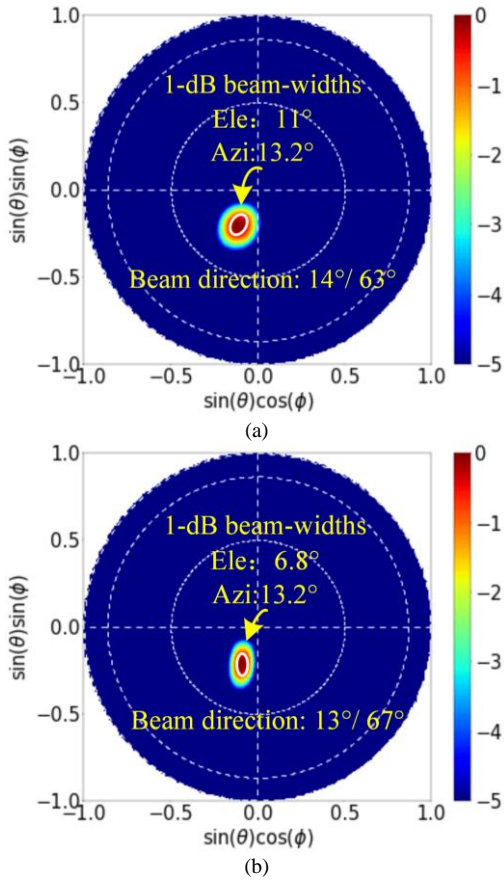


Fig. 12. Simulated 2-D plot of radiation field. (a) 19 GHz; (b) 29 GHz. Unit of color is dB.

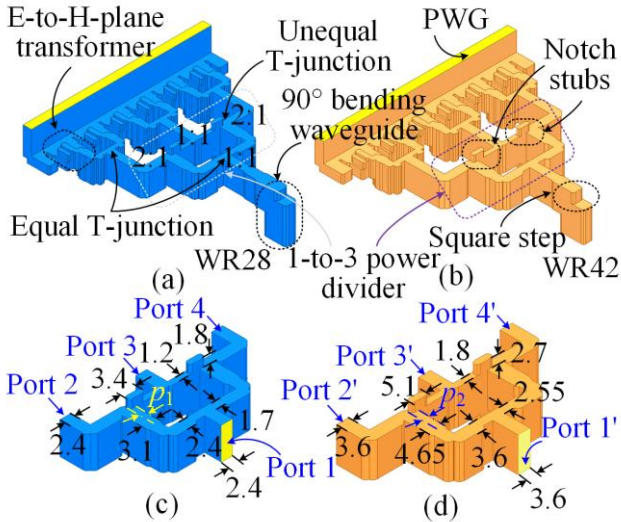


Fig. 13. Structures of PWGs. (a) Tx band; (b) Rx band. All dimensions are given in millimeters.

for both Tx and Rx bands exceeds -45° , which satisfies the design specification. Symmetrical beam coverage can be achieved when the whole antenna rotates 180° . During the beam scanning, a consistent beam direction is achieved in both the elevation and azimuth planes. The maximum deviation of beam direction occurs between 19 GHz and 29 GHz in azimuth plane at $\varphi_1=10^\circ$. This is about 4° . Fig. 12 shows the simulated 2-D plot of the radiated fields. The 1-dB beam-widths are

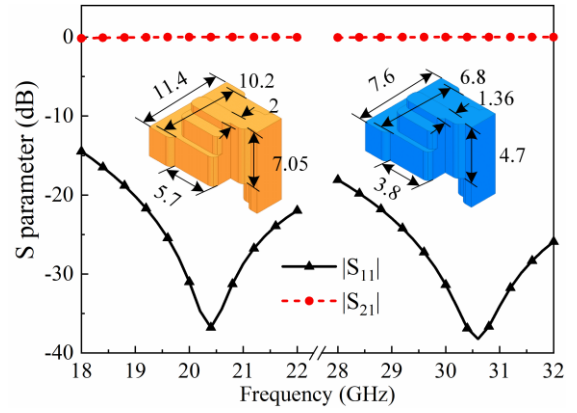


Fig. 14. Simulated reflection coefficients of the E-to-H-plane transformer in Tx and Rx bands. All dimensions are given in millimeters.

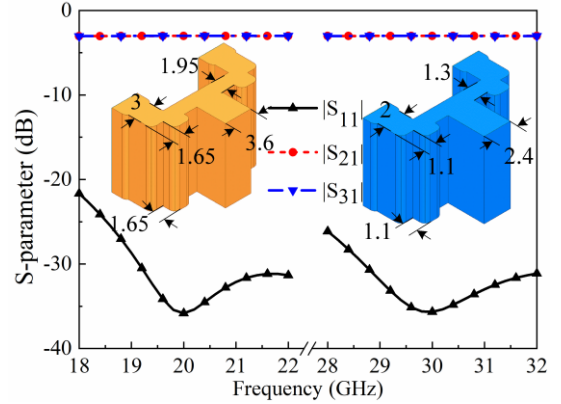


Fig. 15. Simulated S-parameters of the T-junction. All dimensions are given in millimeters.

$11^\circ/13.2^\circ$ and $6.8^\circ/13.2^\circ$ in elevation- and azimuth-planes at 19 GHz and 29 GHz, which ensures the cross-level of the two main beams remains within 1 dB.

C. PWGs

The PWG generates high-quality quasi-TEM wave to feed the CTS radiation slots with non-uniform SWS. Fig. 13 (a) and (b) shows the structure of the PWG in Tx and Rx bands. They are both composed of an E-plane 1-to-6 equal-division power divider cascaded with a multi-port excited PPW structure. The E-plane cut does not disturb the current on the broad wall as much as the H-plane cut does where the contact plane intercepts the current path. This potentially causes radiation leakage. E-plane cut is the more favorable in this sense [39]. Due to the PPW height is not matched with the E-plane T-junction, an E-to-H-plane converter with a three-step twisted waveguide structure is used for the field transition and impedance matching. With the optimized dimensions shown in Fig. 14, the simulated reflection coefficients of the two transformers at Tx and Rx bands are plotted in Fig. 14. $|S_{11}|$ are less than -20 dB in their respective bands. The multiple-port excited PPW structure combines the TE_{10} mode in the H-plane waveguides into the quasi-TEM mode in the PPW. This has been analyzed in our previous work [40] and will not be repeated here.

The E-plane 1-to-6 power divider is realized by using a 1-to-3 power divider cascaded with three T-junctions. All the 1-to-3 power divider and T-junctions have equal-amplitude and

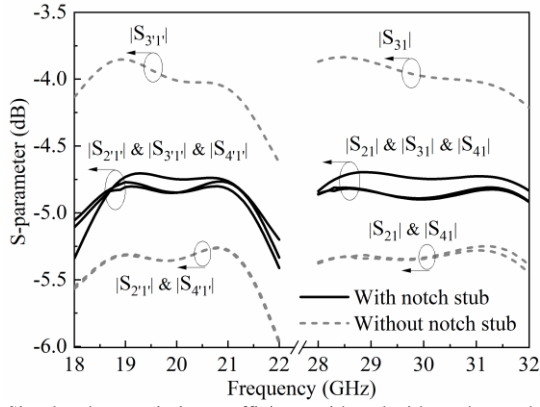


Fig. 16. Simulated transmission coefficients with and without the notch stubs in the 1-to-3 power divider. In the case of with notch stub, $p_1=1.4$ mm and $p_2=1.85$ mm.

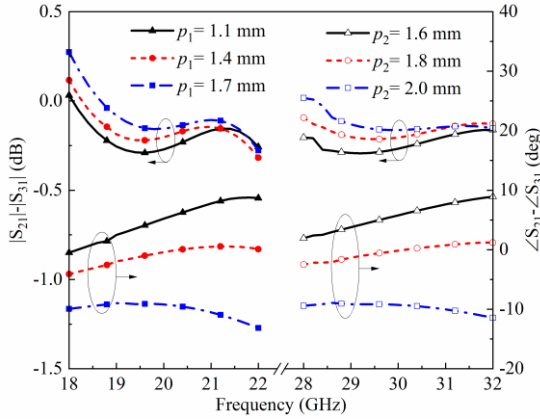


Fig. 17. Simulated amplitude and phase differences among the output ports in the 1-to-3 power divider.

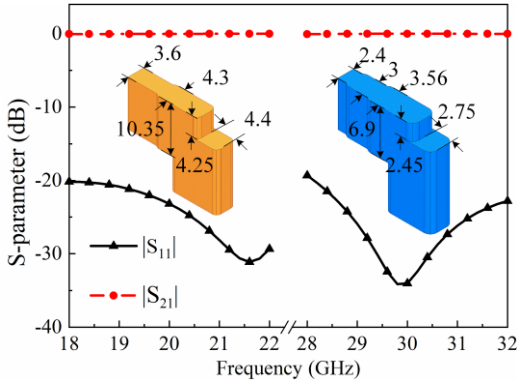


Fig. 18. Simulated reflection coefficients of the transition structure. All dimensions are given in millimeters.

in-phase responses. The simulated results of the T-junctions at the two bands, as well as the optimized dimensions, are shown in Fig. 15. The $|S_{11}|$ are less than -20 dB for both bands. To facilitate the layout, a new compact equal-amplitude and in-phase 1-to-3 power divider structure is adopted, as shown in Fig. 13 (a) and (b). It is the combination of two equal and two unequal T-junctions. The power ratios for each T-junction are also given in Fig. 13 (a). The unequal power ratio is achieved by changing the output branch width. Considering the feasibility of fabrication, the width of the waveguide cannot be too small, limiting the achievable power ratio. A notch stub is therefore added at the unequal T-junction to further increase the

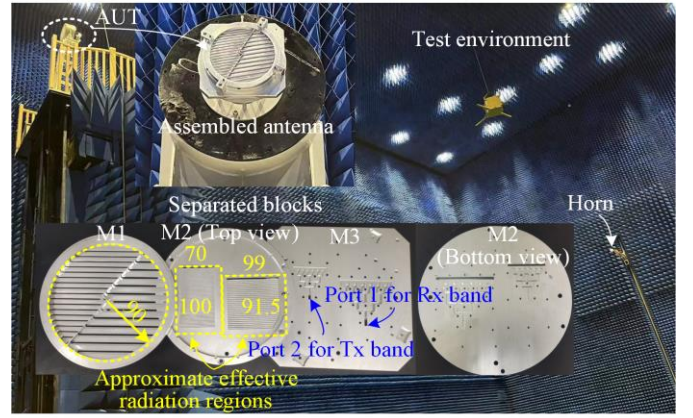


Fig. 19. Photographs of separated metal blocks, assembled antenna and test environment. All dimensions are given in millimeters.

power ratio. Fig. 16 shows the transmission coefficients with and without the notch stubs. When the notch stub is not loaded, the output amplitude of the middle port is smaller than that of the ports on both sides. This is because the power ratio of the unequal division T-junction is less than 2 in this case. With the notch stub, 1-to-3 power divider exhibits the equal-amplitude response. Furthermore, the position of the notch stub can eliminate the phase imbalance caused by the unequal power division structure. Fig. 17 shows the simulated amplitude and phase differences between the ports 3 and 2(4). By adjusting the location of the notch stub (p_1 is for the Tx band and p_2 is for the Rx band, as marked out in Fig. 13 (c) and (d)), the output phase difference can be compensated. When $p_1=1.4$ mm / $p_2=1.85$ mm, the phase difference is reduced to within $\pm 2^\circ / \pm 1.5^\circ$ for Tx and Rx bands, respectively. At the same time, the amplitude differences are within 0.3 dB in both bands.

The 90° bending waveguide structure is used to transition from the standard input waveguide to the E-plane waveguide. The impedance matching can be improved by optimizing the dimensions of the square step at the corner. Fig. 18 shows the simulated reflection coefficients. These are lower than -20 dB.

IV. EXPERIMENTAL RESULTS

The prototype is assembled from three metal blocks for fabrication by milling with a manufacturing tolerance of $20 \mu\text{m}$. It should be noted that the PWG is divided into two parts from the middle of the E-plane waveguide, one part is in the lower half of the block M2, and the other part is in the block M3. Screws around the radiating and feeding parts are used to assemble the antenna and suppress the EM leakage. The photographs of the separated blocks, assembled antenna and the test environment are shown in Fig. 19. The size of the prototype is 180 mm in diameter and 39 mm in height. The effective radiation aperture is considered to be the region covered by the non-uniform SWS. Considering that the excitation signal is not immediately cut off at the boundary of the non-uniform SWS due to the existence of an intermetallic gap for the relative rotational motion, the size of the actual effective radiation region is appropriately increased (also marked out in Fig. 19). The radiation performance is measured using a far-field antenna test system in an anechoic chamber.

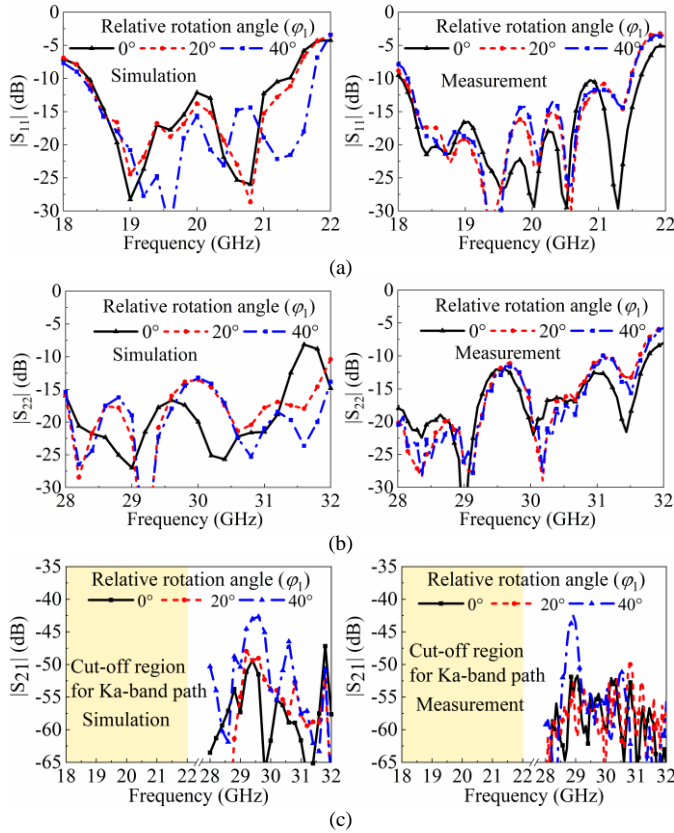


Fig. 20. Simulated and measured S-parameters. (a) $|S_{11}|$ in Rx band; (b) $|S_{22}|$ in Tx band; (c) $|S_{21}|$.

A. Reflection Coefficient

The simulated and measured reflection coefficients at different relative rotation angle in Tx and Rx bands are plotted in Fig. 20(a) and (b), respectively. The measured data is obtained by using an Agilent E8361C network analyzer. Good agreement is achieved between the simulation and measurement results. In the Tx (29-31 GHz) and Rx (19-21 GHz) bands, the measured reflection coefficients are both under -10 dB, exhibiting a stable impedance matching during beam scanning. The simulated and measured isolations between the input ports are shown in Fig. 20(c). Due to the frequency cut-off of waveguide paths for the different frequency bands, only the isolation in overlapping frequency bands (i.e., Tx band) is presented. They are both better than 42 dB.

B. Radiation patterns and Gain

The simulated and measured normalized radiation patterns at different rotation angles in the Tx and Rx bands are presented in Fig. 21. The simulated results agree well with the measured ones. The simulated minimum 1-dB beam-widths are larger than 2.9° during the beam scanning, while the measured one is over 2.7° . These minimum beam-widths appear at the initial beams. The measured beam directions, as well as the simulation values, are listed in Table II. The measured beam directions of the initial beams are all within $\theta=10^\circ$ in elevation plane. At the same time, a consistent beam direction during scanning is achieved in the desired Tx and Rx bands. The maximum measured deviations is 2° (less than half of the corresponding measured 1-dB beam-width) between 19 GHz and 29 GHz at

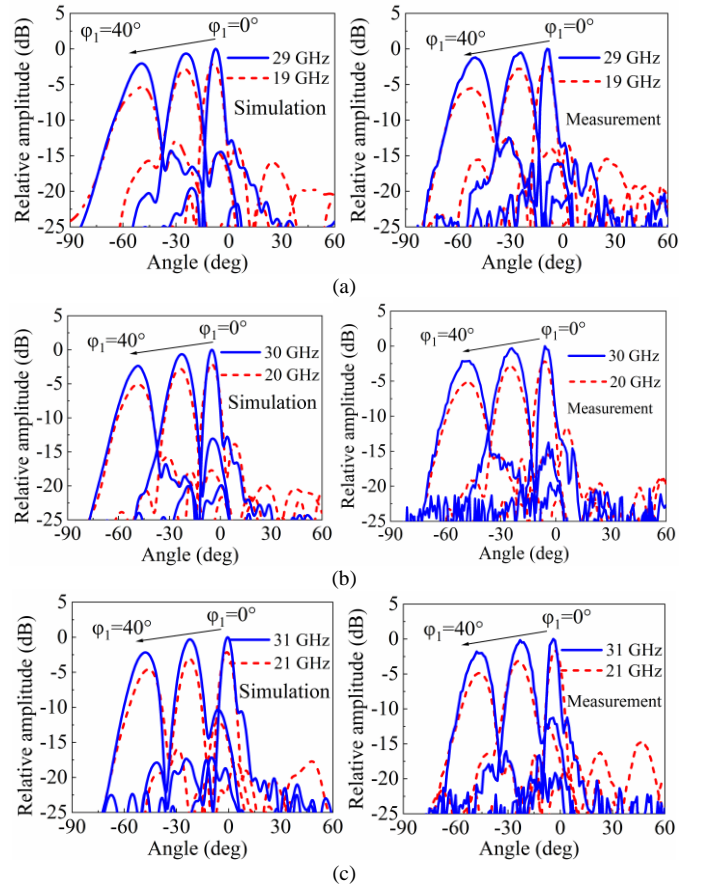


Fig. 21. Simulated and measured normalized radiation patterns at different frequencies. (a) 19 GHz and 29 GHz; (b) 20 GHz and 30 GHz; (c) 21 GHz and 31 GHz.

TABLE II
SIMULATED AND MEASURED BEAM DIRECTIONS IN TX AND RX BANDS

		Measurement		Simulation	
		Ele. plane	Azi. plane	Ele. plane	Azi. plane
19/29 GHz	$\phi_1=0^\circ$	$-9.6^\circ/-9^\circ$	$0^\circ/0^\circ$	$-8.8^\circ/-7.6^\circ$	$0^\circ/0^\circ$
	$\phi_1=20^\circ$	$-25^\circ/-24^\circ$	$80.5^\circ/81^\circ$	$-25.5^\circ/-24.4^\circ$	$79^\circ/80.5^\circ$
	$\phi_1=40^\circ$	$-52^\circ/-50^\circ$	$99.5^\circ/101^\circ$	$-49.5^\circ/-49.2^\circ$	$99^\circ/100.5^\circ$
20/30 GHz	$\phi_1=0^\circ$	$-6^\circ/-6^\circ$	$0^\circ/0^\circ$	$-5.2^\circ/-4.8^\circ$	$0^\circ/0^\circ$
	$\phi_1=20^\circ$	$-25^\circ/-24^\circ$	$88^\circ/86.5^\circ$	$-23.6^\circ/-22.8^\circ$	$86^\circ/86.5^\circ$
	$\phi_1=40^\circ$	$-48^\circ/-47^\circ$	$104^\circ/103^\circ$	$-48.4^\circ/-48.4^\circ$	$102.5^\circ/104^\circ$
21/31 GHz	$\phi_1=0^\circ$	$-2.8^\circ/-4^\circ$	$0^\circ/0^\circ$	$-1.6^\circ/-2.4^\circ$	$0^\circ/0^\circ$
	$\phi_1=20^\circ$	$-24^\circ/-23^\circ$	$95^\circ/93.5^\circ$	$-22.8^\circ/-22^\circ$	$94.5^\circ/93^\circ$
	$\phi_1=40^\circ$	$-47^\circ/-48^\circ$	$106^\circ/106^\circ$	$-46.4^\circ/-47.6^\circ$	$106^\circ/106.5^\circ$

$\phi_1=40^\circ$ in elevation plane. The measured beam directions agree well with the simulated ones. The maximum inconsistency happens at 19 GHz. It is 2.5° in elevation plane at $\phi_1=40^\circ$. This slight difference between the simulated results and measured ones is mainly caused by the manufacturing tolerances, assembly and measurement errors. At $\phi_1=40^\circ$, the beam directions for all frequencies are around $\theta=50^\circ$, exhibiting a wide beam scanning range. The sidelobe level is less than -10 dB during the beam scanning.

Fig. 22 shows the simulated and measured realized gain with different relative rotation angles. The measured peak gain ranges within 23.7 - 20.2 dBi / 25.7 - 24 dBi, 24.1 - 21.3 dBi / 26.3 - 24.1 dBi, and 24.5 - 21.2 dBi / 26.1 - 24.3 dBi at 19/29

TABLE III
PERFORMANCE COMPARISONS OF VICTS ANTENNAS

Ref.	Antenna type	Cent. frequency (GHz)/ FBW (%)	Beam coverage	Aperture size! (λ_0/λ_0^2)	Gain (dBi)	Ape. Efficiency.	Isolation (dB)	Gain drop (dB)	Dual-band operation	Consistent beam direction
[33]	HW-VICTS	12/16%	$\pm 56^\circ$	D=12	30.1	67%	-	7.8	No	No
[34]	HW-VICTS	11.85/15.2%	$\pm 61^\circ$	D=27.65	37.2	60%	-	5	No	No
[35]	HW-VICTS	61.5/13%	$\pm 60^\circ$	D=11.6	29.3	77%	-	4.3	No	No
[36]	HW-VICTS	19.8/3% 29.2/2.7%	$\pm 38^\circ$ $\pm 60^\circ$	L ² : 7.3×6.5 H: 10.8×9.7	24.3 28.5	45.8% 55%	>20	1.6 6.72	Yes	No
This work	HW-VICTS	20/10% 30/6.7%	$\pm 47^\circ$ $\pm 47^\circ$	L ³ : 6.1×6.6 H: 10×7	>21.3 >24.1	65.4% 59.6%	>42	3.5 2.3	Yes	Yes

¹ λ_0 is the free space wavelength at the center frequency of each passband.

²L: Low passband, H: High passband

³These are approximations based on the effective radiation regions shown in Fig. 19.

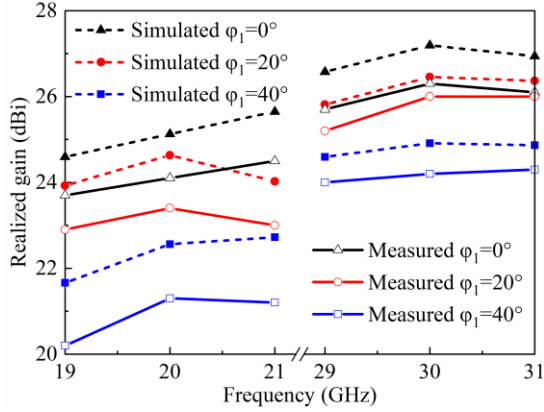


Fig. 22. Simulated and measured peak gains with different ϕ_1 .

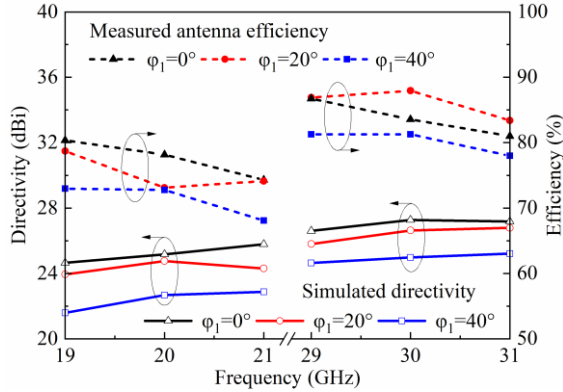


Fig. 23. Simulated directivities and measured antenna efficiencies with different ϕ_1 .

GHz, 20/30 GHz, and 21/31 GHz, respectively. The simulated peak gain is within the ranges of 24.6 - 21.6 dBi / 26.5 - 24.6 dBi, 25.1 - 22.5 dBi / 27.2 - 24.2 dBi, and 25.6 - 22.7 dBi / 26.9 - 24.8 dBi at 19/29 GHz, 20/30 GHz, and 21/31 GHz. The measured peak gain has a maximum 1.5 dB gain drop compared to the simulated one at 21 GHz with $\phi_1=40^\circ$. The measured gain drop during the beam scanning is reduced to within 2.3 dB and 3.5 dB in Tx and Rx bands, which verifies the effectiveness of the pre-deflection (in Section III-B). With the different relative rotation angles, the simulated directivities are shown in Fig. 23. They are in the ranges of 24.6 - 21.6 dBi / 26.6 - 24.6 dBi, 25.1 - 22.6 dBi / 27.3 - 24.9 dBi, and 25.7 - 22.8 dBi / 27.1 - 25.2 dBi at 19/29 GHz, 20/30 GHz, and 21/31 GHz. The measured total antenna efficiency is also shown in Fig. 23. It is calculated by

using the measured realized peak gain and the simulated directivity. During the beam scanning, the measured antenna efficiencies in the Rx and Tx bands are in the range of 68.1 - 80.4% and 78 - 87.8%, respectively. For a specific operating frequency, the antenna efficiency variation is no more than 7.5%. The maximum variation occurs at 19 GHz, and the antenna efficiency is in the range of 72.9 - 80.4% during beam scanning. Based on the simulated directivities of the initial beams and approximated effective radiation apertures shown in Fig. 19, the aperture efficiencies are up to 59.6% and 65.4% at the center frequencies of the Tx and Rx bands, respectively.

C. Comparison With Other Works

Table III shows the performance comparison between this work and some other VICTS antennas. All the works are based on hollow-waveguide (HW). [33], [34], and [35] support single-band operation, while [36] and this work support dual-band shared- or combined-aperture operation. However, [36] did not achieve the beam scanning with consistent beam direction between the Tx and Rx bands. To the best of the authors' knowledge, this work represents the first demonstrated dual-band combined-aperture VICTS antenna with consistent beam directions.

V. CONCLUSION

This paper demonstrated a novel Tx/Rx dual-band combined-aperture VICTS antenna. The topology of the proposed combined-aperture VICTS antenna is derived from the requirement for the consistent beam direction. Non-uniform SWSs are respectively loaded underneath the Tx and Rx parts of the radiation slots to achieve the desired phase relation within a wide frequency band, while the amplitude distributions remain uniform. The pre-deflection technique is further applied in the radiation slots to reduce the gain variation during the beam scanning. A prototype operating at K- and Ka-bands was designed, fabricated and measured. Experimental results show that the initial beam directions in the frequency ranges of 19-21 GHz (Rx band) and 29-31 GHz (Tx band) are all restricted within $\theta=10^\circ$ in elevation plane, and the beam direction exceeds $\pm 47^\circ$ at $\phi_1=40^\circ$. The consistent beam direction is achieved between the Tx and Rx bands during the beam scanning. This design provides a promising solution for LEO SOTM applications.

REFERENCES

- [1] D. Li, S. Wang, H. Zhao and X. Wang, "Context-and-social-aware online beam selection for mmWave vehicular communications," *IEEE Internet Things J.*, vol. 8, no. 10, pp. 8603-8615, May 2021.
- [2] J. Wang, K. Zhu and E. Hossain, "Green internet of vehicles (IoV) in the 6G era: toward sustainable vehicular communications and networking," *IEEE Trans. Green Commun. Netw.*, vol. 6, no. 1, pp. 391-423, Mar. 2022.
- [3] *Solutions for NR to Support Non-Terrestrial Networks (NTN)*, Standard TR 38.821 V16.0.0, 3GPP, Dec. 2019.
- [4] Z. -J. Guo, Z. -C. Hao, H. -Y. Yin, D. -M. Sun and G. Q. Luo, "Planar shared-aperture array antenna with a high isolation for millimeter-wave low earth orbit satellite communication system," *IEEE Trans. Antennas Propag.*, vol. 69, no. 11, pp. 7582-7592, Nov. 2021.
- [5] C. Mao, S. Gao, Y. Wang, Q. Chu and X. Yang, "Dual-band circularly polarized shared-speriture srray for C-/X-Band satellite communications," *IEEE Trans. Antennas Propag.*, vol. 65, no. 10, pp. 5171-5178, Oct. 2017.
- [6] Z. Yang, K. C. Browning and K. F. Warnick, "High-efficiency stacked shorted annular patch antenna feed for Ku-band satellite communications," *IEEE Trans. Antennas Propag.*, vol. 64, no. 6, pp. 2568-2572, June 2016.
- [7] H. Al-Saedi, J. K. Ali, W. M. Abdel-Wahab, S. Gigoyan and S. Safavi-Naeini, "A dual circularly polarized patch antenna for broadband millimeter wave (MMW) communication systems," in *IEEE International Symposium on Antennas and Propagation (APSURSI)*, Fajardo, 2016, pp. 593-594.
- [8] E. Martinez-de-Rioja, J. A. Encinar, R. Florencio and C. Tienda, "3-D bifocal design method for dual-reflectarray configurations with application to multibeam satellite antennas in Ka-band," *IEEE Trans. Antennas Propag.*, vol. 67, no. 1, pp. 450-460, Jan. 2019.
- [9] P. Naseri, S. A. Matos, J. R. Costa, C. A. Fernandes and N. J. G. Fonseca, "Dual-band dual-linear-to-circular polarization converter in transmission mode application to K/Ka-band satellite communications," *IEEE Trans. Antennas Propag.*, vol. 66, no. 12, pp. 7128-7137, Dec. 2018.
- [10] H. Enke and J. Letschnik, "Investigation of Ka-band satcom link performance for teleoperated search and rescue applications," *IEEE Aerosp. Electron. Syst. Mag.*, vol. 34, no. 1, pp. 28-38, Jan. 2019.
- [11] Q. Luo, S. Gao, and L. Zhang, "Millimeter-wave smart antennas for advanced satellite communications," in *Proc. IEEE MTT-S Int. Microw. Symp. (IMS)*, May 2015, pp. 1-4.
- [12] F. Tabarani, L. Boccia, D. Calzona, G. Amendola and H. Schumacher, "Power-efficient full-duplex K/Ka-band phased array front-end," *IET Microw. Antennas Propag.*, vol. 14, no. 4, pp. 268-280, Mar. 2020
- [13] H. Al-Saedi et al., "A low-cost Ka-band circularly polarized passive phased-array antenna for mobile satellite applications," *IEEE Trans. Antennas Propag.*, vol. 67, no. 1, pp. 221-231, Jan. 2019.
- [14] S. A. Matos, J. R. Costa, E. Lima, C. A. Fernandes and N. J. G. Fonseca, "Prototype of a compact mechanically steered Ka-band antenna for satellite on-the-move," in *IEEE International Symposium on Antennas and Propagation (APSURSI)*, Fajardo, 2016, pp. 1487-1488.
- [15] S. Wang, L. Zhu, G. Zhang, J. Yang, J. Wang and W. Wu, "Dual-band dual-CP all-metal antenna with large signal coverage and high isolation over two bands for vehicular communications," *IEEE Trans. Veh. Technol.*, vol. 69, no. 1, pp. 1131-1135, Jan. 2020.
- [16] J. Huang, W. Lin, F. Qiu, C. Jiang, D. Lei and Y. J. Guo, "A low profile, ultra-lightweight, high efficient circularly-polarized antenna array for Ku band satellite applications," *IEEE Access*, vol. 5, pp. 18356-18365, 2017.
- [17] Z. H. Jiang, Y. Zhang and W. Hong, "Anisotropic impedance surface enabled low-profile broadband dual-circularly-polarized multi-beam reflect-arrays for Ka-band applications," *IEEE Trans. Antennas Propag.*, vol. 68, no. 8, pp. 6441-6446, Aug. 2020.
- [18] J. I. Herranz-Herruzo, A. Valero-Nogueira, M. Ferrando-Rocher, B. Bernardo, A. Vila and R. Lenormand, "Low-cost Ka-band switchable RHCP/LHCP antenna array for mobile SATCOM terminal," *IEEE Trans. Antennas Propag.*, vol. 66, no. 5, pp. 2661-2666, May 2018.
- [19] P. Chen, W. Hong, H. Zhang, J. Chen, H. Tang and Z. Chen, "Virtual phase shifter srray and its application on Ku band mobile satellite reception," *IEEE Trans. Antennas Propag.*, vol. 63, no. 4, pp. 1408-1416, Apr. 2015.
- [20] S. Moon, S. Yun, I. Yom and H. L. Lee, "Phased array shaped-beam satellite antenna with boosted-beam control," *IEEE Trans. Antennas Propag.*, vol. 67, no. 12, pp. 7633-7636, Dec. 2019.
- [21] S. A. Matos et al., "High gain dual-band beam-steering transmit array for satcom terminals at Ka-band," *IEEE Trans. Antennas Propag.*, vol. 65, no. 7, pp. 3528-3539, Jul. 2017.
- [22] Y. Jung, A. V. Shishlov and S. Park, "Cassegrain antenna with hybrid beam steering scheme for mobile satellite communications," *IEEE Trans. Antennas Propag.*, vol. 57, no. 5, pp. 1367-1372, May 2009.
- [23] S. Qu, S. Lu, C. Ma and S. Yang, "K/Ka dual-band reflectarray subreflector for ring-focus reflector antenna," *IEEE Antennas Wireless Propag. Lett.*, vol. 18, no. 8, pp. 1567-1571, Aug. 2019.
- [24] Y. Gao, T. Hong, W. Jiang, S. Gong and F. Li, "Low-profile wideband CTS array using substrate-integrated waveguide technology for K-band applications," *IEEE Trans. Antennas Propag.*, vol. 67, no. 8, pp. 5711-5716, Aug. 2019.
- [25] T. Potelon, M. Ettorre, L. Le Coq, T. Bateman, J. Francey and R. Sauleau, "Reconfigurable CTS antenna fully integrated in PCB technology for 5G backhaul applications," *IEEE Trans. Antennas Propag.*, vol. 67, no. 6, pp. 3609-3618, Jun. 2019.
- [26] X. Lu, S. Gu, X. Wang, H. Liu and W. Lu, "Beam-scanning continuous transverse stub antenna fed by a ridged waveguide slot array," *IEEE Antennas Wireless Propag. Lett.*, vol. 16, pp. 1675-1678, 2017.
- [27] T. Lou, X.-X. Yang, H. Qiu, Z. Yin, and S. Gao, "Compact dual polarized continuous transverse stub array with 2-D beam scanning," *IEEE Trans. Antennas Propag.*, vol. 67, no. 5, pp. 3000-3010, May 2019.
- [28] Y. You, Y. Lu, Q. You, Y. Wang, J. Huang and M. J. Lancaster, "Millimeter-wave high-gain frequency-scanned antenna based on waveguide continuous transverse stubs," *IEEE Trans. Antennas Propag.*, vol. 66, no. 11, pp. 6370-6375, Nov. 2018.
- [29] M. Del Mastro et al., "Analysis of circularly polarized CTS srrays," *IEEE Trans. Antennas Propag.*, vol. 68, no. 6, pp. 4571-4582, Jun. 2020.
- [30] W. W. Milroy, S. B. Coppedge, and A. C. Lemons, "Variable inclination continuous transverse stub array," U. S. Patent 6919854, 2005.
- [31] M. Wei, J. Liu, H. Li and S. Liu, "Design of a variable inclination continuous transverse stub array," in *12th International Symposium on Antennas, Propagation and EM Theory (ISAPE)*, Hangzhou, China, 2018, pp. 1-3.
- [32] B. G. Porter, "Closed form expression for antenna patterns of the variable inclination continuous transverse stub," in *IEEE International Symposium on Phased Array Systems and Technology*, Waltham, MA, 2010, pp. 164-169.
- [33] A. Wang, L. Yang, X. Yi, X. Li, J. Zhao, and Y. Zhang, "Wireless communication applications of the variable inclination continuous transverse stub array for Ku-band applications," *IET Microw. Antennas Propag.*, vol. 15, no. 6, pp. 644-652, Mar. 2021.
- [34] M.-Y. Zhao, X. Lei, J. Gao, Y.-J. Zhu, T.-P. Li, and Q. Peng, "A two-dimensional beam scanning continuous transverse stub antenna based on a single-layer compact linear source generator," *IET Microw. Antennas Propag.*, vol. 15, no. 14, pp. 1842-1852, Oct. 2021.
- [35] K. Tekkouk, J. Hirokawa, R. Sauleau and M. Ando, "Wideband and large coverage continuous beam steering antenna in the 60-GHz band," *IEEE Trans. Antennas Propag.*, vol. 65, no. 9, pp. 4418-4426, Sep. 2017.
- [36] R. S. Hao, Y. J. Cheng and Y. F. Wu, "Shared-aperture variable inclination continuous transverse stub antenna working at K- and Ka-band for mobile satellite communication," *IEEE Trans. Antennas Propag.*, vol. 68, no. 9, pp. 6656-6666, Sep. 2020.
- [37] A. Bhattacharyya, "Theory of beam scanning for slot array antenna excited by slow wave," *IEEE Antennas Propag. Mag.*, vol. 57, no. 2, pp. 96-103, Apr. 2015.
- [38] N. Mehra, A. Kakkar and S. C. Bera, "System design aspects of Ka-band high throughput satellite (HTS) for Indian region," in *Twenty Fourth National Conference on Communications (NCC)*, Hyderabad, India, 2018, pp. 1-6
- [39] Z. Shi-Gang, H. Guan-Long, P. Zhao-hang and L. Ying, "A wideband full-corporate-feed waveguide slot planar array," *IEEE Trans. Antennas Propag.*, vol. 64, no. 5, pp. 1974-1978, May 2016.
- [40] Y. You, Y. Lu, Y. Wang, J. Xu, J. Huang and W. Hong, "Enhanced pencil-beam scanning CTS leaky-wave antenna based on meander delay line," *IEEE Antennas Wireless Propag. Lett.*, vol. 20, no. 9, pp. 1760-1764, Sep. 2021.